Self-interaction correction in multiple scattering theory: application to transition metal oxides

Self-interaction correction in multiple scattering theory: application to transition metal oxides

M Däne[1,2]**, M Lüders**[3]**, A Ernst**[4]**, D Ködderitzsch**[5]**,**
W M Temmerman[3]**, Z Szotek**[3] **and W Hergert**[1]

[1] Institut für Physik, Martin-Luther-Universität Halle-Wittenberg, Von-Seckendorff-Platz 1,
D-06120 Halle, Germany
[2] Materials Science and Technology Division, Oak Ridge National Laboratory, Oak Ridge,
TN 37831, USA
[3] Daresbury Laboratory, Daresbury, Warrington WA4 4AD, UK
[4] Max Planck Institut für Mikrostrukturphysik, Weinberg 2, D-06120 Halle, Germany
[5] Ludwig-Maximilians-Universität München, Physikalische Chemie, Butenandtstraße 11,
D-81377 München, Germany

E-mail: markus.daene@physik.uni-halle.de

Abstract
We apply to transition metal monoxides the self-interaction corrected (SIC) local spin density
approximation, implemented locally in the multiple scattering theory within the
Korringa–Kohn–Rostoker (KKR) band structure method. The calculated electronic structure
and in particular magnetic moments and energy gaps are discussed in reference to the earlier
SIC results obtained within the linear muffin-tin orbital atomic sphere approximation band
structure method, involving transformations between Bloch and Wannier representations, in
order to solve the eigenvalue problem and calculate the SIC charge and potential. Since the
KKR method can be easily extended to treat disordered alloys, by invoking the coherent
potential approximation (CPA), in this paper we compare the CPA approach and supercell
calculations to study the electronic structure of NiO with cation vacancies.

(Some figures in this article are in colour only in the electronic version)

1. Introduction

Density functional theory (DFT) forms the basis of most
first-principles electronic structure calculations of solids [1].
In particular, the commonly used local (spin) density
approximation (L(S)DA) to DFT has been extremely
successful in describing bonding properties of solids,
especially the conventional metals and their alloys. However,
due to the local approximation, describing correlations at the
level of the homogeneous electron gas, LSDA (LSD: local
spin density) or even the semi-local, generalized gradient
approximation (GGA) often fails for systems like transition
metal monoxides (TMOs) containing partially filled TM d-
shells. The same is true for rare earths and heavier actinides
and their compounds, where the f-shells are partially filled. It
is the strong Coulomb repulsion among the electrons in those
partially filled d- and f-shells that is not well represented within
LSDA and GGA. For TMOs, LSDA either fails to describe
their insulating ground state or predicts much too small band
gaps and magnetic moments [2–4]. This is associated with an
unphysical self-interaction of an electron with itself, occurring
in the Hartree term of the LSDA energy functional on account
of the local approximation applied to the exchange–correlation
energy functional. This self-interaction becomes important
for localized electrons like d electrons of TM elements in
their monoxides. In the latter, the self-interactions push
the localized electron orbitals into the valence band, usually
resulting in too strong a hybridization with the other valence
electrons. This problem was recognized many years ago
and a remedy was proposed by Perdew and Zunger [5] to
simply subtract the spurious self-interactions from the LSDA
functional, orbital by orbital, for all the localized states.

The resulting SIC–LSDA approach treats both localized and itinerant electrons on equal footing, leading to split d- and f-manifolds and describing the dual character of an electron.

The SIC–LSDA method has been successfully applied to numerous systems containing localized d and/or f electrons [6–16]. In most cases the so-called full SIC (FSIC) implementation was used [17, 18], involving repeated transformations between Bloch and Wannier representations to, respectively, solve the generalized eigenvalue problem, and calculate orbital dependent charges and potentials. Since the self-interaction correction is *local* in nature with the electronic states affected by SIC localized to a high degree on a site, the so-called local SIC (LSIC) has recently been implemented and successfully applied to some f electron materials [15, 16]. This LSIC approach, taking advantage of multiple scattering theory, has been implemented within the Korringa–Kohn–Rostoker (KKR) band structure method, which offers straightforward generalizations to treating various types of chemical, charge and spin disorder through the coherent potential approximation (CPA) and disordered local moments (DLM) [19] theory. Due to an easy access to the Green's function, the KKR method is also well suited for studying surfaces, interfaces and other low dimensional systems. Finally, the LSIC implementation in KKR allows for finite temperature calculations and therefore is very useful for studying finite temperature phase diagrams [15].

The motivation for the present paper is to explore the consequences of applying LSIC to study the ground state properties of TMOs. The latter are the prototypical d electron materials for studying strong correlation effects and have been extensively studied both experimentally and theoretically by a number of methods [7, 20–25]. One of the goals of this paper is to demonstrate that the LSIC scheme can be as successfully applied to systems containing localized 3d electrons, as it was for the systems with localized 4f electrons. In the case of TMOs, these are the 3d electrons of the transition metal elements that are affected by SIC.

As already mentioned, a number of theoretical methods have been used to study TMOs the most popular being the LDA + U method [20, 26–28]. It treats Coulomb interactions between electrons better than LSDA, by explicitly adding to the LSDA Hamiltonian a Hubbard term with the on-site Coulomb interaction U. The latter is usually treated as an adjustable parameter and chosen to optimize agreement with experiment. For TMOs, the approach works well and for NiO, with the appropriate choice of the U parameter, the results have been shown to be in very good agreement with those of the FSIC approach [21]. The LDA + U method has also been applied to study surface properties of NiO [29, 30] and MnO [31], as well as exchange interactions in some TMOs [31, 32]. Besides LDA + U and SIC schemes, a class of hybrid functionals has recently been introduced. These functionals treat Coulomb correlations beyond LSDA, accomplished by incorporating some fraction of the exact exchange. The most well known among them is the B3LYP functional [33]. There have been a number of recent applications of various hybrid functionals to TMOs [22–25].

Whereas all the above mentioned approaches provide a static treatment of the correlation problem, the dynamical mean field theory (DMFT) [34, 35] allows to systematically include local dynamical correlations into lattice models. However, most applications to date invoke the Hubbard Hamiltonian, via the so-called LDA + DMFT implementation, and thus inherit the uncertainties associated with the LDA + U method. Recent LDA + DMFT calculations [36] for NiO, with a suitable choice of U, provide good agreement with angle resolved photoemission spectroscopy. Finally, the GW method, in various implementations, has also been used to study TMOs [37–40]. However, the degree of its success depends on the starting band structure and the LDA band structure is a poor starting point.

The paper is organized as follows. In section 2, we elaborate on the local implementation of the SIC formalism within the KKR band structure method. In section 3, numerical details of the calculations are discussed. Section 4 is devoted to an extensive discussion of the LSIC results for NiO to demonstrate LSIC at work. In section 5, we review the ground state properties of all the 3d TMOs studied with LSIC, in comparison with experiment and the early FSIC results. In section 6, we consider cation vacancies in NiO using CPA, in addition to the earlier supercell study within the full SIC implementation [10]. The paper is summarized in section 7.

2. Formalism

2.1. Basic SIC–LSDA equations

To present the basics of the SIC–LSDA method, we start from the LSDA total energy functional, in the Kohn–Sham representation [1], which is (in Rydberg units) given by

$$E^{\text{LSDA}}[n_\uparrow, n_\downarrow] = \sum_\alpha^{\text{occ}} \langle \phi_\alpha | - \nabla^2 | \phi_\alpha \rangle + E_{\text{ext}}[n]$$
$$+ E_{\text{H}}[n] + E_{\text{xc}}^{\text{LSDA}}[\bar{n}], \tag{1}$$

where ϕ_αs are the Kohn–Sham orbitals, giving rise to the orbital densities $n_\alpha = |\phi_\alpha|^2$, with α being a combined index labelling the orbital and spin σ ($\uparrow$ or $\downarrow$), $\bar{n}$ stands for the spin densities $n_\uparrow, n_\downarrow$, and the total density is defined as $n = n_\uparrow + n_\downarrow$. Here E_{ext} is the external potential energy functional due to ions, E_{H} is the Hartree energy functional

$$E_{\text{H}}[n] = \int \text{d}^3 r \int \text{d}^3 r' \, \frac{n(\mathbf{r})n(\mathbf{r}')}{|\mathbf{r} - \mathbf{r}'|}, \tag{2}$$

and $E_{\text{xc}}^{\text{LSDA}}$ is the LSD approximation to the exchange–correlation energy functional, which is the source of the spurious self-interaction [5]. The exact exchange–correlation energy has the property that it cancels exactly the Hartree energy for any single-electron density n_α, namely

$$E_{\text{H}}[n_\alpha] + E_{\text{xc}}^{\text{exact}}[\bar{n}_\alpha] = 0, \tag{3}$$

where $\bar{n}_\alpha$ represents the pair of spin densities $(n_\alpha, 0)$ or $(0, n_\alpha)$, depending on the spin σ of the state α. Correcting the LSDA energy functional for the unphysical self-interaction error, by subtracting explicitly the self-Coulomb and self-exchange and self-correlation energy of all the occupied orbitals, restores

the above property, but leads to an orbital dependent energy functional

$$E^{\text{SIC-LSDA}}[\{n_\alpha\}] = \tilde{E}^{\text{LSDA}}[\bar{n}]$$
$$- \sum_\alpha^{\text{occ}} (E_{\text{H}}[n_\alpha] + E_{\text{xc}}^{\text{LSDA}}[\bar{n}_\alpha]), \tag{4}$$

with $\tilde{E}^{\text{LSDA}}[n_\uparrow, n_\downarrow]$ having the same form as $E^{\text{LSDA}}[n_\uparrow, n_\downarrow]$, however, the orbitals setting up the orbital densities, n_α, in equation (4) are no longer the usual Kohn–Sham orbitals. The latter are replaced by $\tilde{\phi}_\alpha$ orbitals that minimize the self-interaction corrected energy functional. Varying the above SIC–LSDA energy functional with respect to the orbital spin densities, with the constraint that the $\tilde{\phi}_\alpha$s form a set of orthonormal functions, one gets the SIC–LSDA generalized eigenvalue equations

$$H_\alpha|\tilde{\phi}_\alpha\rangle = \left(-\nabla^2 + V_{\text{eff},\alpha\sigma}^{\text{SIC-LSDA}}(\mathbf{r})\right)|\tilde{\phi}_\alpha\rangle$$
$$= \left(H_{0\sigma} + V_\alpha^{\text{SIC}}(\mathbf{r})\right)|\tilde{\phi}_\alpha\rangle = \sum_{\alpha'} \lambda_{\alpha\alpha'}|\tilde{\phi}_{\alpha'}\rangle, \tag{5}$$

with $H_{0\sigma}$ being the orbital independent LSDA Hamiltonian. The Lagrangian multipliers $\lambda_{\alpha\alpha'}$ are used to secure the fulfilment of the orthonormality constraint. Due to the orbital dependent potential, the SIC energy functional is not stationary with respect to infinitesimal unitary transformations among the orbitals. The so-called localization criterion

$$\langle\tilde{\phi}_\beta|V_\alpha^{\text{SIC}} - V_\beta^{\text{SIC}}|\tilde{\phi}_\alpha\rangle = 0 \qquad \forall(\alpha, \beta) \tag{6}$$

has to be fulfilled to ensure that the solutions of the SIC–LSDA equations (5) are most optimally localized to reach the absolute minimum of the SIC–LSDA functional (4).

The orbital dependent potential $V_{\text{eff},\alpha\sigma}^{\text{SIC-LSDA}}$ is given by

$$V_{\text{eff},\alpha\sigma}^{\text{SIC-LSDA}}(\mathbf{r}) = \underbrace{V_{\text{ext}}(\mathbf{r}) + V_{\text{H}}[n](\mathbf{r}) + V_{\text{xc}\sigma}^{\text{LSDA}}[\bar{n}](\mathbf{r})}_{V_{\text{eff},\sigma}^{\text{LSDA}}}$$
$$- \underbrace{V_{\text{H}}[n_\alpha](\mathbf{r}) - V_{\text{xc},\sigma}^{\text{LSDA}}[\bar{n}_\alpha](\mathbf{r})}_{V_\alpha^{\text{SIC}}(\mathbf{r})}, \tag{7}$$

the external lattice potential $V_{\text{ext}}(\mathbf{r})$, and

$$V_{\text{H}}[n](\mathbf{r}) = 2\int \text{d}^3 r' \frac{n(\mathbf{r}')}{|\mathbf{r} - \mathbf{r}'|}, \tag{8}$$

$$V_{\text{xc},\sigma}^{\text{LSDA}}[n_\uparrow, n_\downarrow](\mathbf{r}) = \frac{\delta E_{\text{xc}}^{\text{LSDA}}[n_\uparrow, n_\downarrow]}{\delta n_\sigma}. \tag{9}$$

In order to implement the above SIC–LSDA methodology, and solve the underlying generalized eigenvalue equations, one can either choose the direct minimization of the energy functional (4) with respect to orbitals, using the steepest descent method [6, 18], or the so-called unified Hamiltonian formulation [7, 18]. Both approaches have been implemented within the linear muffin-tin orbital (LMTO) band structure method in the atomic sphere approximation (ASA) [41, 42], i.e., both approaches start from the band representation of the electronic structure. This, as mentioned earlier, means that repeated transformations between the Bloch representation, to solve the generalized eigenvalue problem, and the Wannier representation, to calculate n_α and construct $V_\alpha^{\text{SIC}}(\mathbf{r})$, have

to be invoked in every step of the self-consistency cycle. It is this change of representations which complicates the self-consistency problem of the self-interaction corrected LSDA. The technical details of these SIC–LSDA implementations, referred to as FSIC, can be found elsewhere [18].

2.2. Multiple scattering theory and LSIC implementation

The so-called 'local' implementation of the SIC–LSDA methodology, in the framework of multiple scattering theory, has already been discussed by Lüders *et al* [15]. Here we repeat the main concepts and formulae for completeness. The important difference of this LSIC implementation, with respect to the FSIC approach, is working with the scattering phase shifts, describing scattering properties of the individual atoms in a solid, treated within multiple scattering theory implemented in the Korringa–Kohn–Rostoker (KKR) method. Core electron states, represented as bound states at negative energies, are characterized by abrupt jumps by π of their generalized complex phase shifts at those energies. The localized valence states, like e.g. 3d electron states in transition metal elements, also show sharp jumps by π but at positive energies, referred to as resonances. The itinerant states, on the other hand, are characterized by slowly varying phase shifts. The idea behind the *local* implementation of SIC–LSDA in the KKR band structure method is to associate SIC with the on-site scattering potential through modifying the corresponding resonant scattering phase shifts. It is the realization of this idea that lies at the heart of LSIC scheme.

The central quantity of the multiple scattering theory is the Green's function which for the scalar-relativistic case is given by

$$G_\sigma(\mathbf{r}, \mathbf{r}'; \epsilon) = \sum_{LL'} \bar{Z}_{L\sigma}^i(\mathbf{r}_i; \epsilon)\, \tau_{\sigma LL'}^{ij}(\epsilon)\, Z_{L'\sigma}^j(\mathbf{r}_j'; \epsilon)$$
$$- \sum_L \bar{Z}_{L\sigma}^i(\mathbf{r}_<; \epsilon)J_{L\sigma}^i(\mathbf{r}_>; \epsilon)\delta_{ij}. \tag{10}$$

Here $\mathbf{r}$ is given by $\mathbf{r} = \mathbf{R}_i + \mathbf{r}_i$, where $\mathbf{r}_i$ is a vector inside the cell at $\mathbf{R}_i$, $L = (l, m)$ denotes the combined index for the angular momentum l and magnetic m quantum numbers, while $\mathbf{r}_<(\mathbf{r}_>)$ is the vector smaller (larger) in magnitude from the pair $(\mathbf{r}, \mathbf{r}')$. The functions $\bar{Z}_{L\sigma}^i$, $Z_{L\sigma}^i$, $J_{L\sigma}^i$ are expressed by the regular ($Z_{L\sigma}^i$) and irregular ($J_{L\sigma}^i$) solutions of the radial Schrödinger equation at a given (complex) energy ϵ and the complex spherical harmonics $Y_L(\hat{\mathbf{r}})$ as

$$Z_{L\sigma}^i(\mathbf{r}_i; \epsilon) = Z_{l\sigma}^i(r_i; \epsilon)Y_L(\hat{\mathbf{r}}_i) \tag{11}$$

$$\bar{Z}_{L\sigma}^i(\mathbf{r}_i; \epsilon) = Z_{l\sigma}^i(r_i; \epsilon)Y_L^*(\hat{\mathbf{r}}_i) \tag{12}$$

$$J_{L\sigma}^i(\mathbf{r}_i; \epsilon) = J_{l\sigma}^i(r_i; \epsilon)Y_L(\hat{\mathbf{r}}_i). \tag{13}$$

The scattering-path matrix $\underline{\tau}$ is given by

$$\underline{\tau}(\epsilon) = \left[\underline{t}^{-1}(\epsilon) - \underline{g}(\epsilon)\right]^{-1}, \tag{14}$$

where the underlined symbols stand for matrices in angular momentum, L, and atomic site indices. The structural Green's function, $\underline{g}(\epsilon)$, describes the free propagation between the scattering centres, and the $\underline{t}$ matrix denotes the single-site

scattering and is related to the phase shifts, δ_l^i, discussed above, via

$$t_l^i(\epsilon) = -\frac{1}{\kappa} \sin \delta_l^i(\epsilon) e^{i\delta_l^i(\epsilon)}, \qquad (15)$$

with κ equal to $\sqrt{\epsilon}$.

The total valence charge density, per spin σ, can be calculated from the Green's function as

$$n_\sigma(\mathbf{r}) = -\frac{1}{\pi} \int_{E_B}^{E_F} d\epsilon \ \text{Im} \ G_\sigma(\mathbf{r}, \mathbf{r}; \epsilon), \qquad (16)$$

where E_B and E_F denote the bottom of the valence band and the Fermi energy, respectively. In the standard LSDA calculations, this charge density is used to construct the new effective potential $V_{\text{eff},\sigma}^{\text{LSDA}}$ (cf equation (7)) for the next iteration of the self-consistency cycle.

In the SIC–LSDA method, one aims to extract from equation (16) those contributions which originate from localized electron states, characterized by sharp resonances in the scattering phase shifts and therefore long Wigner delay times, as they will be associated with large self-interaction errors. These are the scattering states to which SIC will be applied. Since the angular momentum decomposition used in (10) is adapted to spherical symmetry, we need to work in the representation which reflects the local symmetry of the scattering centre under consideration. To accomplish this, we apply a unitary transformation to the spherical harmonics in the angular momentum decomposition, such that the angular momentum diagonal block of the on-site scattering-path matrix becomes diagonal. This unitary transformation is defined by

$$\sum_{m_1, m_2} U_{(l\tilde{m}, lm_1)}^\dagger \underline{\tau}_{(lm_1, lm_2)}^{ii}(\epsilon) U_{(lm_2, l\tilde{m}')} = \delta_{\tilde{m}\tilde{m}'} \underline{\tilde{\tau}}_{\tilde{L}, \tilde{L}'}^{ii}(\epsilon), \quad (17)$$

while the regular solution in this symmetry adapted representation assumes the form

$$Z_{\tilde{L}\sigma}^i(\mathbf{r}_i; \epsilon) = \sum_{m_1} U_{(l\tilde{m}, lm_1)}^\dagger \{Z_{lm_1\sigma}^i(r_i; \epsilon) Y_{lm_1}(\hat{\mathbf{r}}_i)\}, \qquad (18)$$

and similarly for the irregular solution. This corresponds to an expansion into lattice harmonics, i.e., linear combinations of spherical harmonics of the same quantum number l, forming the basis functions of the respective irreducible representations.

Due to the employed muffin-tin or atomic sphere approximation in KKR, only the spherically symmetric parts of the SIC charges and potentials are considered. Because of this, only the spherical part of the Green's function matters, which in the symmetrized representation becomes diagonal with respect to $\tilde{L} = (l, \tilde{m})$, which defines the so-called scattering channel. Hence, we can decompose the spin resolved charge density (equation (16)) into its $\tilde{L}$ components and define the charge of a given channel, characterized by its site index i, symmetry index $\tilde{L}$ and spin σ, as

$$n_{i\tilde{L}\sigma}^{\text{SIC}}(\mathbf{r}) = -\frac{1}{\pi} \int_{E_1}^{E_2} d\epsilon \ \text{Im} \ G_{\tilde{L},\sigma}(\mathbf{r}, \mathbf{r}; \epsilon), \qquad (19)$$

where the energies E_1 and E_2 lie, respectively, slightly below and above the energy of the resonance in the channel $\tilde{L}\sigma$

at site i. In principle, the integration range should enclose the localized state only, but for simplicity we use the energy contour encompassing the whole valence band, namely ranging from the bottom of the valence band to the Fermi energy. From these channel densities, we can construct the corresponding SIC potentials, which together with the LSDA potential, define the effective SIC–LSDA potential, namely

$$V_{\text{eff},i\tilde{L}\sigma}^{\text{SIC-LSDA}}(\mathbf{r}) = V_{\text{eff},\sigma}^{\text{LSDA}}(\mathbf{r}) - V_H[n_{i\tilde{L}\sigma}^{\text{SIC}}](\mathbf{r}) - V_{\text{xc}}^{\text{LSDA}}[n_{i\tilde{L}\sigma}^{\text{SIC}}, 0](\mathbf{r}).$$
$$(20)$$

This gives rise to the single scattering matrix of the form

$$t_{\tilde{L}\sigma}^{i,\text{corr}} = t_{\tilde{L}\sigma}^i(1 - \delta_{\tilde{L},\tilde{L}^c}\delta_{\sigma,\sigma^c}) + t_{\tilde{L}^c\sigma}^{i,\text{SIC-LSDA}}\delta_{\tilde{L},\tilde{L}^c}\delta_{\sigma,\sigma^c}, \quad (21)$$

with some of the channels, marked by $\tilde{L}^c\sigma^c$, being self-interaction corrected, and $t_{\tilde{L}\sigma}^i$ being the t-matrix calculated from the effective LSDA potential, $V_{\text{eff},\sigma}^{\text{LSDA}}(\mathbf{r})$. Here $t_{\tilde{L}\sigma}^{i,\text{SIC-LSDA}}$ is calculated from the effective SI-corrected LSDA potential, $V_{\text{eff},i\tilde{L}\sigma}^{\text{SIC-LSDA}}(\mathbf{r})$. The corrected t^{corr}-matrix is then used in equation (14) to calculate the new, SI-corrected, scattering-path matrix $\underline{\tilde{\tau}}$. From the latter the new SIC–LSDA charge density is calculated, and the process is iterated until self-consistency is reached. Since we are dealing with resonances, the localization criterion used for optimizing Wannier orbitals in FSIC, giving rise to the additional self-consistency cycle, is not in operation in LSIC.

One of the important advantages of the SIC–LSDA formalism is that one can realize and study different valence configurations of the elements under consideration, and this is valid for both FSIC and LSIC schemes. The nominal valence, N_{val}, is defined as

$$N_{\text{val}} = Z - N_{\text{core}} - N_{\text{SIC}}, \qquad (22)$$

where Z is the atomic number, N_{core} is the number of core (and semicore) states and N_{SIC} is the number of self-interaction corrected states. The ground state valence is the one defined by the ground state energy. One has to mention that it has to be tested which states need to be corrected (e.g. equation (21)) in order to find the ground state and the ground state valency. How it is done in practice will be demonstrated for NiO in section 4.

Finally, as already mentioned, the multiple scattering formulation of SIC, naturally lends itself to various extensions like the coherent potential approximation (CPA), [43–46] allowing study of random alloys, within the resulting KKR–CPA method. In section 6, we will discuss an application of LSIC, in combination with CPA, to study the influence of vacancies on the Ni-sublattice in NiO on its electronic structure.

3. Computational details

The 3d transition metal monoxides crystallize in the rocksalt structure (B1, $Fm\bar{3}m$, space group 225), consisting of two fcc sublattices, shifted with respect to each other by $[a/2, 0, 0]$. One of the sublattices is occupied by the oxygen atoms and the other one by the transition metal

elements. At low temperatures, TMOs show a small ($<2\%$) lattice distortion, which is rhombohedral for MnO, FeO and NiO (cf [47]), but tetragonal for CoO [48]. In this paper, however, we do not consider these lattice distortions. Above the transition temperature, the structure of TMOs is cubic. The ground state magnetic structure is of the antiferromagnetic type II (AFII) [49], originating from Anderson-type superexchange. The AFII structure consists of an antiferromagnetic stacking of (111) planes, of parallel moments, along the [111] direction. The oxygen atoms are frustrated by symmetry, so that they do not contribute to the total magnetic moment. To realize the AFII structure in the calculations, a unit cell consisting of two formula units was used. The crystal potentials of the TMO systems used in the LSIC calculations were constructed based on the atomic sphere approximation (ASA). The ASA radii of the TM and oxygen atoms were chosen to be equal, because the LSIC results were not crucially dependent on the relative division of space between the various species. In addition, the so-called empty spheres were used to obtain a better space filling, as well as to minimize the effect of the ASA overlap. The actual ASA radii for TM and oxygen atoms were chosen to be $0.2895a$ and for empty spheres $0.1774a$, with a being the lattice parameter of a given compound.

The analytical expression for the KKR Green's function given by equation (10) is exact in the limit of $L = (l, m) \to \infty$, and can be evaluated at any energy. In practice, however, a reasonable cut-off in the angular momentum summations has to be imposed, which in all the calculations presented in this paper was $l_{max} = 3$, for all the sites. For the oxygen atoms, the 2s states were treated as valence states since they form extended Bloch states. Regarding energy integrals, they were performed in the complex plane and the contour used was a semi-circle, with points on the contour chosen using the Gaussian quadrature. In most cases, 32 energy points were used. The integrals over the Brillouin zone were performed using a special k-points method.

Finally, a comment on the use of Lloyd's formula in all the calculations of this paper. Since the LSIC approach is based on the calculation of the Green's functions, such quantities as density of states (DOS), integrated density of states, Fermi energy, charge density, total charge, as well as other observables, are evaluated from these Green's functions by the appropriate integrations. We know from experience that the Fermi energy evaluated from the integrated DOS, obtained by integrating the imaginary part of the Green's function over space and energy, is not accurate due to slow angular momentum convergence, and may give rise to systematic errors for semiconductors and insulators. To avoid such errors one can use Lloyd's formula [50], which allows direct calculation of the differences between the integrated densities of states of the system under consideration and some properly chosen reference system, leading to much more accurate Fermi energies in particular for semiconductors and insulators. Details of an efficient implementation of Lloyd's formula used in all the calculations presented here have been presented elsewhere [51].

4. Application to NiO

In this section we demonstrate, using NiO as an example, how LSIC operates in practice. NiO is very probably the most studied system among the transition metal monoxides, both experimentally and theoretically. The earliest SIC–LSDA applications to NiO, as well as other TMOs [6, 7], based on the FSIC approach, assumed the AFII magnetic order and obtained a good description of its electronic structure, with a considerably large energy band gap and much improved magnetic moments as compared to LSDA. In a later study of NiO, using a larger set of LMTO basis functions as well as much improved space filling and reduced ASA overlap error due to the introduction of the so-called empty spheres, a good description of the bonding properties, band gap, magnetic properties and EELS spectra was obtained, in agreement with experiment and an LDA + U calculation, with a reasonable value of U [21]. That the AFII structure was not crucial for the FSIC calculations to obtain an insulating state in NiO was shown by Ködderitzsch *et al* [9] who considered different magnetic orders and in particular AFII, AFI and ferromagnetic (FM) structures. The AFI structure is characterized by an antiferromagnetic stacking of ferromagnetic Ni planes along the [100] direction. For all the studied magnetic orders, an insulating solution with a substantial band gap was obtained [9], unlike in the case of LSDA, where neither AFI nor FM states could be stabilized, and for the AFII scenario, only a tiny band gap was obtained. Based on these total energy calculations and mapping onto a Heisenberg model, Ködderitzsch *et al* [9] also calculated exchange interactions of bulk NiO and at the NiO(100) surface, and found them to be in good agreement with experiment. Recently, by combining LSIC with DLM, it has also been shown that in NiO, the energy band gap survives above the Néel temperature, with the value not much different than the one obtained for the ground state AFII structure [52]. Although the magnitude of the band gap, calculated using SIC, seems to be slightly affected by the type of magnetic order due to the apparent change in hybridization between the Ni 3d bands and predominantly oxygen 2p-like valence band, it is not the exchange field but the on-site Coulomb repulsion that drives the insulating state in NiO and other TMOs. Therefore, in the remainder of this section we shall concentrate solely on the electronic structure and magnetic moments calculated from LSIC for the ground state, AFII, structure of bulk NiO.

From ionic considerations, it is obvious that Ni-ion in NiO will have 2^+ valency. In a solid state the 2^+ valency can be realized in a number of different ways depending on the crystal field splittings. In the bulk NiO, Ni-ions are octahedrally coordinated and the Ni d bands, due to the resulting crystal field, are split into the t_{2g} and e_g subbands, with the capacity of accommodating respectively three and two electrons, separately for the spin-up and spin-down channels. Among the t_{2g} and e_g band states one can identify orbitals of different symmetry and they are associated with the same angular momentum, l, but different magnetic, m, quantum numbers. Using the Cartesian nomenclature, the symmetries of the three states belonging to the t_{2g} set are d_{xy}, d_{yz} and

Table 1. The summary of all studied 2^+ and 3^+ SIC configurations, specifying the spin and symmetry of the chosen localized orbitals for each. The two digits separated by a hyphen in the first column identify the configurations. The first digit denotes the valency and the other simply numbers the consecutive configurations within a given valence group, namely separately for the divalent and trivalent sets.

Config.	Valency	Choice of orbitals
2-1	2^+	$3t_{2g}\uparrow + 2e_g\uparrow + 3t_{2g}\downarrow$
2-2	2^+	$3t_{2g}\uparrow + 2e_g\uparrow + 2t_{2g}\downarrow + 1e_g\downarrow$
2-3	2^+	$3t_{2g}\uparrow + 1e_g\uparrow + 3t_{2g}\downarrow + 1e_g\downarrow$
2-4	2^+	$3t_{2g}\uparrow + 2e_g\uparrow + 1t_{2g}\downarrow + 2e_g\downarrow$
2-5	2^+	$3t_{2g}\uparrow + 1e_g\uparrow + 2t_{2g}\downarrow + 2e_g\downarrow$
2-6	2^+	$2t_{2g}\uparrow + 2e_g\uparrow + 2t_{2g}\downarrow + 2e_g\downarrow$
3-1	3^+	$3t_{2g}\uparrow + 2e_g\uparrow + 2t_{2g}\downarrow$
3-2	3^+	$2t_{2g}\uparrow + 2e_g\uparrow + 3t_{2g}\downarrow$
3-3	3^+	$3t_{2g}\uparrow + 1e_g\uparrow + 3t_{2g}\downarrow$
3-4	3^+	$3t_{2g}\uparrow + 2e_g\uparrow + 1t_{2g}\downarrow + 1e_g\downarrow$
3-5	3^+	$2t_{2g}\uparrow + 2e_g\uparrow + 2t_{2g}\downarrow + 1e_g\downarrow$
3-6	3^+	$3t_{2g}\uparrow + 1e_g\uparrow + 2t_{2g}\downarrow + 1e_g\downarrow$
3-7	3^+	$3t_{2g}\uparrow + 2e_g\uparrow + 2t_{2g}\downarrow$
3-8	3^+	$3t_{2g}\uparrow + 1e_g\uparrow + 1t_{2g}\downarrow + 2e_g\downarrow$
3-9	3^+	$2t_{2g}\uparrow + 2e_g\uparrow + 1t_{2g}\downarrow + 2e_g\downarrow$

Figure 1. Total energies of different SIC configurations in NiO calculated as a function of the lattice constant. The energy zero is set to the 'global' minimum among the different configurations. The lowest energy is found for the high symmetry state $(3\,t_{2g}\uparrow + 2e_g\uparrow + 3t_{2g}\downarrow)$, resulting in the valency of 2^+.

d_{zx}, while the two e_g states are referred to as $d_{x^2-y^2}$ and $d_{3z^2-r^2}$, for both spin-up and spin-down channels. Of course, as we have spherical potentials and work in the symmetry adapted representation, all the states within a given subband are energetically equivalent. Thus in what follows we refer only to t_{2g}s and e_gs for both spin channels. Based on this, one can consider localized orbitals of different symmetry and spin and for these orbitals the self-interaction correction is implemented when describing their electronic structure. In the LSIC formulation there are the resonant phase shifts associated with these localized d states that define the scattering channels to be self-interaction corrected. With respect to different valency states, one can realize them by varying the number of localized d states, e.g. for a divalent Ni-ion one would consider eight localized d electrons, but only seven for a trivalent ion. For the monovalent Ni-ion one would need to assume nine localized d electron states, which however is hard to stabilize as far as self-consistency is concerned.

As mentioned earlier, the SIC–LSDA functional is not stationary with respect to mixing among the orbitals and different sets of orbitals will lead to different SIC. Thus one has to study different configurations of localized orbitals and minimize the SIC–LSDA total energy with respect to these configurations to find the ground state energy and valence. Naturally, one needs to consider not only different symmetries of the localized orbitals, but also configurations with different numbers of localized orbitals, giving rise to different valence states. The reason is that some valence states may lie close in energy and valence transitions may readily occur e.g. as a function of pressure. For NiO all the studied configurations of localized states, namely six giving rise to the 2^+ valence and nine resulting in 3^+ valence, are given in table 1.

In order to find the ground state total energy, equilibrium volume and valence state, we have performed LSIC calculations for all the configurations listed in table 1. The results are presented in figure 1, where the total energy
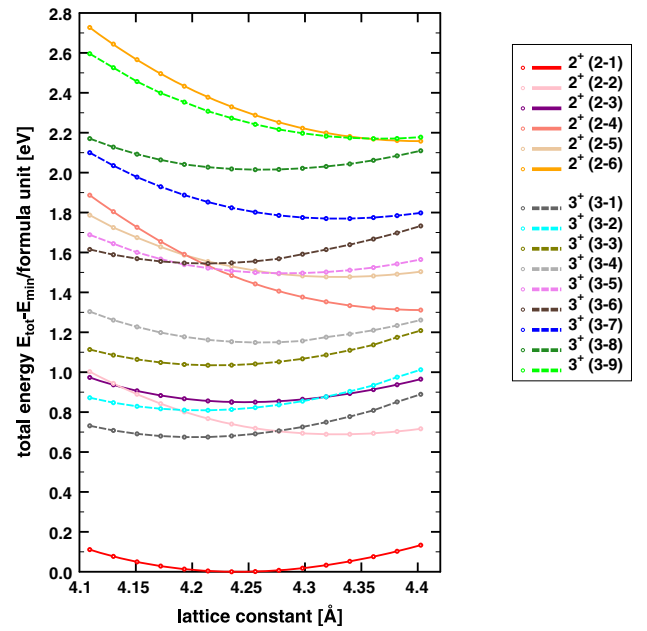
curves are plotted for all the configurations as a function of lattice constants. The equilibrium lattice constants of all the configurations are defined by the minima of the corresponding energy curves. Specifically, the energies are plotted relative to the global energy minimum, the 2^+ state, obtained when the five majority Ni ds and three minority Ni t_{2g} states are occupied and treated as localized [(2-1)]. This result is in agreement with the FSIC calculations [6, 7, 21] and reflects the first Hund's rule in maximizing the spin magnetic moment. This Hund's rule ground state is very robust and well separated in energy with respect to the other 14 curves seen in figure 1, showing that in the lowest energy configuration, the Ni d states are very well localized, nearly atomic-like, in the sense that they even obey Hund's rules. Furthermore, the robustness of this Hund's rule driven ground state comes about due to the crystal field splitting and the resulting preference to fill the lower lying t_{2g} states first.

Looking at the remaining 14 curves in figure 1, we can observe many valence transitions between divalent and trivalent states as a function of pressure. The general observation, for all the studied configurations, is that the configurations which follow the first Hund's rule in maximizing the spin moment, independently within the t_{2g} and e_g subbands, have usually lower energies than the configurations violating this rule. This can be easily seen in table 2, where all the configurations are listed in the order starting from the most energetically favourable to most energetically unfavourable, separately for the divalent and trivalent scenarios. Among the configurations with equal number of t_{2g} states occupied, the configurations giving rise to higher magnetic moments have in general lower energies.

Table 2. The summary of the main characteristics of all the studied 2^+ and 3^+ SIC configurations in NiO (cf figure 1). The six 2^+ configurations appear as the top six rows and are marked by two digits separated by a hyphen. The first digit is always '2', marking the valence, while the second one changes from 1 to 6, marking the order in which the 2^+ configurations appear in the legend of figure 1. The larger the digit, the more energetically unfavourable the configuration is. For the 3^+ configurations, the first digit is naturally '3', while the second one changes from 1 to 9, again corresponding to the order in which these configurations appear in the legend of the figure, reflecting the gradual decrease in energy preference. Here ΔE denotes the total energy differences per formula unit relative to the total energy of the ground state configuration marked as 2-1. Δa gives the relative shift (in per cent) of the equilibrium lattice constants of all the configurations with respect to the equilibrium lattice parameter of the ground state configuration. The valency column is followed by the columns giving the total numbers of localized states, separately for the $(t_{2g}\uparrow, t_{2g}\downarrow)$ and $(e_g\uparrow, e_g\downarrow)$ subbands. Finally, the corresponding spin moments for the two subbands, as well as the total one, are also given.

Config.	ΔE (eV)	Δa (%)	Valency	Localized electrons t_{2g}	e_g	Moments t_{2g}	e_g	Tot.
2-1	0.00	±0.00	2^+	6 (3, 3)	2 (2, 0)	0	2 ↑	2 ↑
2-2	0.69	+2.05	2^+	5 (3, 2)	3 (2, 1)	1 ↑	1 ↑	2 ↑
2-3	0.84	+0.14	2^+	6 (3, 3)	2 (1, 1)	0	0	0
2-4	1.31	+4.03	2^+	4 (3, 1)	4 (2, 2)	2 ↑	0	2 ↑
2-5	1.47	+2.12	2^+	5 (3, 2)	3 (1, 2)	1 ↑	1 ↓	0
2-6	2.16	+3.93	2^+	4 (2, 2)	4 (2, 2)	0	0	0
3-1	0.67	−0.90	3^+	5 (3, 2)	2 (2, 0)	1 ↑	2 ↑	3 ↑
3-2	0.81	−0.78	3^+	5 (2, 3)	2 (2, 0)	1 ↓	2 ↑	1 ↑
3-3	1.03	−0.46	3^+	6 (3, 3)	1 (1, 0)	0	1 ↑	1 ↑
3-4	1.15	+0.37	3^+	4 (3, 1)	3 (2, 1)	2 ↑	1 ↑	3 ↑
3-5	1.50	+0.99	3^+	4 (2, 2)	3 (2, 1)	0	1 ↑	1 ↑
3-6	1.55	−0.68	3^+	5 (3, 2)	2 (1, 1)	1 ↑	0	1 ↑
3-7	1.77	+2.10	3^+	3 (3, 0)	4 (2, 2)	3 ↑	0	3 ↑
3-8	2.01	+0.48	3^+	4 (3, 1)	3 (1, 2)	2 ↑	1 ↓	1 ↑
3-9	2.17	+2.97	3^+	3 (2, 1)	4 (2, 2)	1 ↑	0	1 ↑

Also, within the configurations with the same number of localized d states, the ones that have more localized t_{2g} states than e_g states have generally lower energies.

Inspecting both figure 1 and table 2, one can see that there is quite a strong dependence of the lattice parameter on the type of the configuration. Among the 2^+ configurations the tendency for the larger lattice constants is observed. Among the 3^+ valence configurations, we observe no clear preference as some of them have smaller and others larger lattice constants. In general, configurations with a complete filling of e_g subbands show a strong dependence of their total energies on the lattice parameter with an apparent shift towards larger lattice parameters.

As can be seen in figure 2, there exists some sensitivity to the equilibrium lattice parameter of the amount of charge associated with a selected scattering channel for which the SIC is applied. The charge is calculated using equation (19), and from this the SIC potential of the given channel is obtained and added to the effective LSDA potential. One should remember that in LSIC these charges are calculated only within the atomic sphere corresponding to the site of the selected channel. Thus, it is likely that, as seen in the figure, charges of less than one electron per channel will be obtained. This is unlike in the
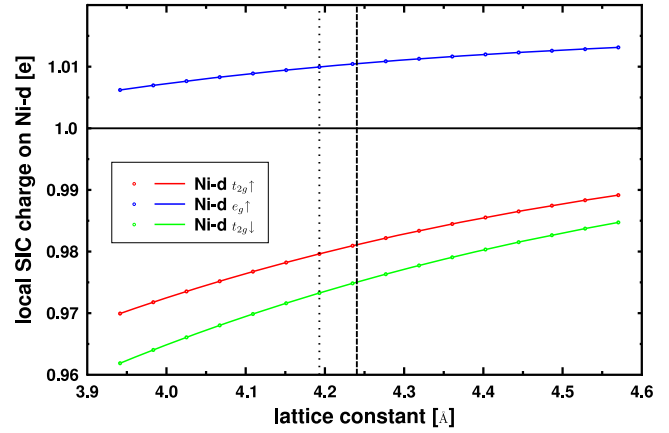

Figure 2. The SIC charges, per channel, for the Ni t_{2g} and e_g states corresponding to the ground state configuration of NiO as a function of lattice constant. The vertical lines denote the experimental (dotted) and theoretical (dashed) lattice constants, respectively.

FSIC approach where the charges of the orbitals considered for SIC are calculated from exponentially decaying Wannier functions optimized on a large cluster of atoms surrounding a given site. In such a case, charges very close to or even of exactly one electron are obtained. In the LSIC approach, we get slightly less than one electron for the majority and minority Ni t_{2g}-channels, but more than one electron for the majority e_g channel. The latter is caused by hybridization with the oxygen 2s and 2p channels as demonstrated in figure 3, showing respectively the phase shifts of both majority and minority Ni t_{2g} and e_g channels, and the corresponding DOS and integrated DOS. In particular, the latter (see figure 3(c)) shows that indeed there is a small contribution to the SIC charge of the majority e_g state due to the aforementioned hybridization. This behaviour might also be elucidated based on the analysis of molecular orbitals (MOs). An MO with the e_g symmetry constructed from the oxygen environment of a given cation and the e_g state at this cation site will have more hybridized character than the MOs with the t_{2g} symmetry.

The phase shifts displayed in figure 3(a) characterize the scattering properties of the constituent atoms in the system. The stronger the scatterer, the more resonant are the phase shifts, as seen for the Ni d states. In the LSD approximation due to the spherical symmetry of the scattering potential, there is only one phase shift associated with all the Ni d electrons (see figure 3(a)). The situation is different in the SIC approach due to the orbital dependent potential breaking the symmetry. By applying SIC to the specific scattering channels, here the Ni d states, their respective phase shifts get shifted downwards in energy and the resonances sharpen up considerably as compared to the LSDA counterparts (figure 3(a)). This agrees well with the physical picture of localization and a long Wigner delay time for such SIC states. However, these states do not become quasi-bound states because their resonances, after applying the SI correction, still lie well above the muffin-tin zero. The positions of these resonances coincide with the respective d peaks in the DOS (figure 3(b)). As can be seen in the figure, the e_g resonance lies lower in energy than the t_{2g}
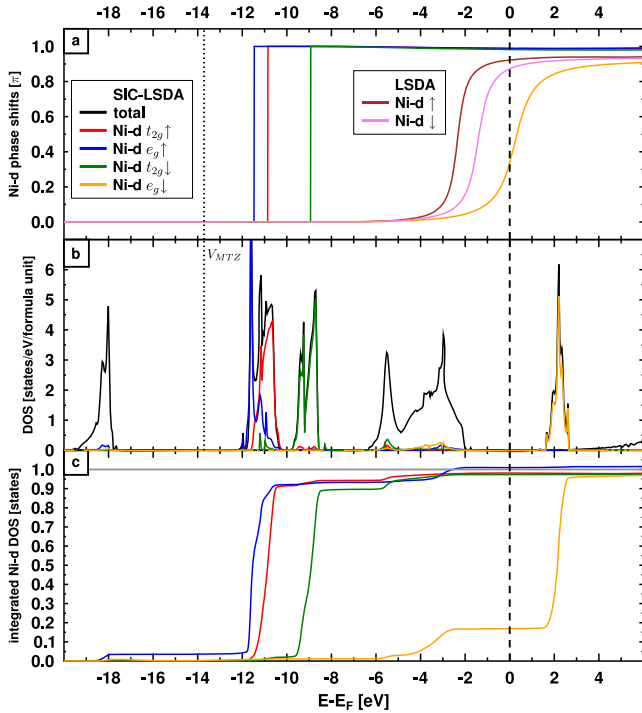
Figure 3. The phase shifts, densities of states, and integrated densities of states at the experimental lattice constant of NiO. Here (a) shows the Ni d phase shifts calculated within LSDA and SIC–LSDA. The LSDA phase shifts (brown/violet) are degenerate for all the *m* channels, the SIC–LSDA phase shifts split due to the orbital dependent potential (breaking LSDA symmetry). The muffin-tin zero V_{MTZ} is marked. In (b) the total DOS (black), together with the symmetry resolved partial DOS of the Ni 3d states, is presented. Panel (c) displays the integrated density of all the Ni d states. The colour scheme is identical in all the subfigures.

Figure 4. The symmetry resolved partial DOS of the self-interaction corrected 3d electron states of Ni: (a) the LSDA calculation, (b) FSIC (LMTO), (c) LSIC (KKR), and (d) LSIC (KKR) where the Slater transition state concept has been implemented.

resonance due to a more attractive SIC potential resulting from a larger SIC charge (see figure 2). The shift of the occupied d states down in energy is associated with an effective upward shift of the unoccupied states, giving rise to opening up of a considerable charge transfer band gap seen in figure 3(b). This is in line with experiment and contrary to the LSDA band gap which is of the Mott–Hubbard-type (see figure 4). The latter, as already discussed by Terakura *et al* [2] is the result of a small exchange splitting which is comparable to a small crystal field splitting. The width of the e_g band is crucial in stabilizing the AFII structure in LSDA because the band gap opens up between the t_{2g} and e_g bands.

In figure 4 (panels (a), (b), and (c)), we present the total and Ni d densities of states for NiO, calculated in the LSD approximation as well as from the FSIC and LSIC approaches for the ground state configuration (figure 1 and table 2). Contrary to LSDA where all the Ni d bands are found around a tiny band gap, in both the LSIC and FSIC approaches the occupied $t_{2g}^{\uparrow}$, $t_{2g}^{\downarrow}$, and $e_g^{\uparrow}$ bands have moved to higher binding energies and have become narrower as a result of the applied self-interaction corrections. Another effect of SIC is the observed considerable change in the crystal field splitting as compared to LSD. From figures 4(b) and (c) one can see that the band gaps, relative positions of different bands, and their hybridizations agree between both
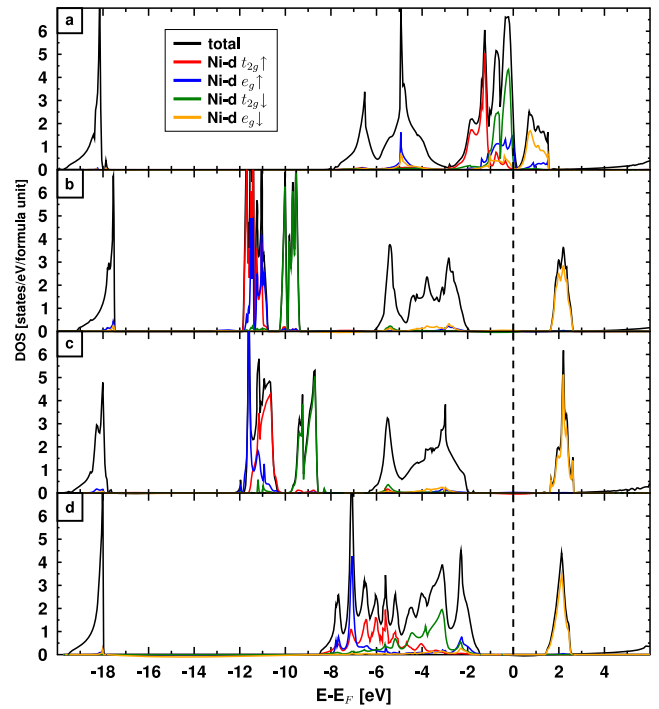
the FSIC and LSIC implementations. The slight shifts in the positions of the SIC d bands may arise from such details like, e.g., possible small differences in the calculated SIC charges. In any case, a fully quantitative agreement cannot be expected due to the completely different implementations of the two SIC approaches, and this is in addition to the different numerical accuracies of the two band structure methods used for these two implementations. It is reassuring, however, that despite these apparent differences in both the FSIC and LSIC implementations, the most relevant trends in DOS and band gaps are correctly reproduced in both approaches.

Regarding comparison of the LSIC and FSIC results with experiment, one has to keep in mind that they are primarily total energy ground state approaches. Whilst the band gaps calculated using SIC–LSDA are of the correct charge transfer character [53, 54], the latter is substantially overestimated. The reason is that the calculated removal energies of the localized Ni d states do not agree with the photoemission spectroscopy, lying a few eV lower in energy than observed experimentally. Consequently, there is not enough Ni d character hybridized into the predominantly O p valence band. Now, a question arises whether one can expect correct removal energies from such an effective one electron ground state theory like SIC–LSDA. Although DFT is, strictly speaking, a theory of the ground state from which spectroscopic information is not easily extracted, the LDA based band structure is often compared to photoemission experiments. This is because the effective Kohn–Sham potentials can be viewed as an energy independent self-energy and hence the Kohn–Sham energy bands correspond to the

mean field approximation for the spectral function. In the
SIC–LSDA, this argument only applies to the itinerant states
that are not self-interaction corrected. The localized states
that have been self-interaction corrected respond to a different
potential [55] and the solution to the generalized SIC–LSDA
eigenvalue problem, which is different from the solution to
the Kohn–Sham equations in the LDA, no longer corresponds
to a mean field approximation of the spectral function [56].
To extract spectroscopic information for the localized states,
one needs to take into account screening/relaxation effects.
One of the well known approaches is to perform the so-
called Δ_{SCF} calculations [57], where one has to compute total
energies of the systems with N, $N-1$, and $N+1$ electrons
which, however, is computationally non-trivial. To obtain
electron removal energies for the localized Ni d states just from
the self-consistent ground state calculation, a transition state
concept [58] can be used. According to this approximation, the
removal energy of a Ni d state is defined as the average of the
calculated SIC–LSDA and LSDA d state expectation values,
formally

$$\overline{\epsilon_{TS}} = \tfrac{1}{2}(\langle d|H_{LSDA} + V_{SIC}|d\rangle + \langle d|H_{LSDA}|d\rangle). \qquad (23)$$

In effect, the SIC potential is only counted with half of its
strength in the transition state approximation to the removal
energies. The transition state concept was implemented by
Filippetti and Spaldin [59], albeit in a different manner, by
invoking the averaging factor of $\tfrac{1}{2}$ already in the total energy
functional. To compare with photoemission spectra, one can
implement equation (23) after the self-consistency has been
reached in the step of calculating the densities of states, we
have done this for NiO.

In figure 4(d) we show the LSIC DOS obtained for the
NiO ground state configuration with the transition state concept
implemented. The corresponding Bloch spectral function
is presented in figure 5. Although the calculations for the
Bloch spectral function have been performed for the complex
energies with a small constant imaginary part, the figure shows
a well resolved band structure, albeit with a small smearing,
along a number of symmetry directions in the Brillouin zone
of the AFII structure. The density of states calculated in the
transition state approximation shows considerably hybridized
valence band with a substantial amount of Ni d character
at the top of the valence band, thus correcting for the SIC
overestimate of the charge transfer character of the band gap
(compare figures 4(b)–(d)). This strong hybridization effect is
also seen in the band structure of figure 5. The unoccupied
minority Ni e_g states are very slightly hybridized with the
O p states. Still, it is rather amazing to see how localized
the unoccupied Ni d states are, considering that no SIC is
implemented for unoccupied band states. Of course, there
exists an indirect effect of SIC on the unoccupied bands due
to the fact that the potential they respond to is the LSDA
effective potential calculated from the charge density of all
the occupied states, of which some have been self-interaction
corrected, notably all the occupied Ni 3d states. However, the
flatness of these two minority Ni e_g bands is a consequence of
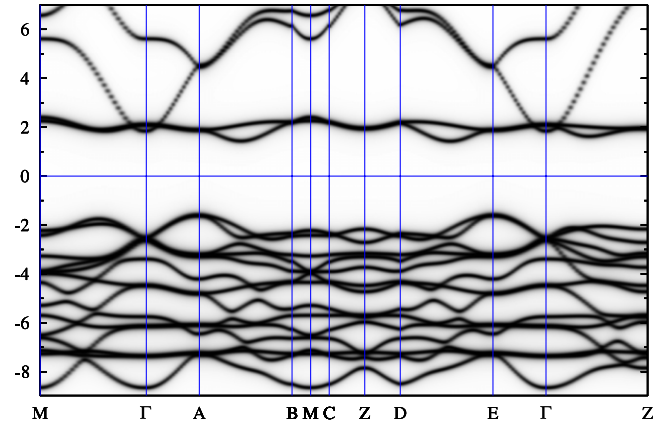the considerably reduced phase space for hybridization.

Figure 5. The calculated Bloch spectral function, corresponding to
the Slater transition state concept along a number of symmetry lines
in the AFII Brillouin zone, giving rise to a well resolved band
structure of NiO. The visible small smearing of bands is due to a
small imaginary part of energies in the calculations.

Table 3. SIC configurations minimizing the total energy for the
series of 3d transition metal oxides.

Compound	SIC configuration
MnO	$3t_{2g}^{\uparrow} + 2e_g^{\uparrow}$
FeO	$3t_{2g}^{\uparrow} + 2e_g^{\uparrow} + 1t_{2g}^{\downarrow}$
CoO	$3t_{2g}^{\uparrow} + 2e_g^{\uparrow} + 2t_{2g}^{\downarrow}$
NiO	$3t_{2g}^{\uparrow} + 2e_g^{\uparrow} + 3t_{2g}^{\downarrow}$
CuO	$3t_{2g}^{\uparrow} + 2e_g^{\uparrow} + 3t_{2g}^{\downarrow} + 1e_g^{\downarrow}$

5. TMO series

In this section we discuss the LSIC results obtained for the
whole TMO series. We restrict the discussion to the ground
state configurations and properties of these compounds. These
ground state configurations lead to the ground state energies
given in table 3. As in the case of NiO, these energy
minimizing configurations satisfy the first Hund's rule. The
way they come about may be understood based on simple
physical considerations. For example, in MnO the exchange
splitting on the Mn site is much larger than the ligand field
splitting, and therefore all five Mn d electrons occupy fully the
majority d band, namely the three $t_{2g}^{\uparrow}$ and two $e_g^{\uparrow}$ band states,
leaving the minority bands empty. For the other compounds in
the series, the additional d electrons start filling the minority
subband with one minority t_{2g} state in FeO, two in CoO, and
all three in NiO; while in CuO, in addition the first minority e_g
state is also filled, as seen in table 3.

The results for the equilibrium lattice constants and the
corresponding magnetic moments and band gaps calculated
with LSIC for all the TMO series are summarized in table 4
and compared with the LSDA values and the experimental
data. Also, the results of much earlier FSIC (LMTO–
ASA) calculations are quoted, mostly for a qualitative
comparison [6, 7]. The reason is that in those calculations,
minimal basis sets were used and no so-called empty spheres
were considered for improving space filling. To make the
comparison more quantitative and meaningful, for NiO we
also present results of later, more numerically advanced FSIC

Table 4. The equilibrium lattice constants, local magnetic moments and the band gaps for the 3d transition metal monoxides calculated with LSIC–KKR and compared to two full SIC–LMTO implementations as well as experimental results. The values for the band gap quoted in the parenthesis are calculated at the experimental lattice constant. The calculated magnetic moments are spin moments only, the experimental values are total moments, including orbital contributions which are known to be substantial for FeO and CoO, and non-negligible even for NiO.

	Compound				
	MnO	FeO	CoO	NiO	CuO
Lattice constant (Å)					
LSDA (KKR)	4.27	4.13	4.05	4.01	4.08
LSIC (KKR)	4.49	4.39	4.31	4.24	4.27
FSIC (LMTO) [21]				4.18	
Expt.	4.446[a], 4.44[b]	4.326[c]	4.26[b,d]	4.176[e], 4.17[b]	4.245[d]
Local magnetic moment on TM (μ_B)					
LSDA (KKR)	4.11 (4.27)	3.26 (3.40)	2.20 (2.33)	0.85 (0.97)	0.00 (0.00)
LSIC (KKR)	4.63 (4.61)	3.68 (3.66)	2.69 (2.68)	1.68 (1.67)	0.76 (0.76)
Expt. (total)	4.79[k], 4.58[l]	3.32[m]	3.35[f], 3.8[m]	1.77[k], 1.90[m], 2.20[g]	0.65[n]
FSIC (LMTO) [6]	4.49	3.54	2.53	1.53	0.65
FSIC (LMTO) [7]	4.64	3.55	2.59	1.49	0.64
FSIC (LMTO) [21]				1.61	
Band gap (eV)					
LSDA (KKR)	0.83 (0.73)	0.00 (0.00)	0.00 (0.00)	0.23 (0.23)	0.00 (0.00)
LSIC (KKR)	3.07 (3.25)	3.38 (3.54)	2.78 (2.81)	3.56 (3.76)	2.52 (2.57)
Expt.	3.6–3.8[o]	2.4[h], 2.5[i]	2.4[p]	4.3[q], 4.0[r], 4.3[j]	1.37[s]
FSIC (LMTO) [6]	3.98	3.07	2.81	2.54	1.43
FSIC (LMTO) [7]	3.57	3.25	2.51	2.66	1.00
FSIC (LMTO) [21]				3.15	

[a] Reference [63]. [b] Reference [64].
[c] Reference [65]. [d] Reference [66].
[e] Reference [67]. [f] Reference [60].
[g] Reference [61]. [h] Reference [68].
[i] Reference [69]. [j] Reference [53].
[k] Reference [70]. [l] Reference [71].
[m] Reference [72]. [n] Reference [73].
[o] Reference [74]. [p] Reference [75].
[q] Reference [76]. [r] Reference [77].
[s] Reference [78].

(LMTO–ASA) calculations [21]. In addition, and for an easy overview, the LSIC results are plotted in figure 6, together with the LSDA (KKR) and experimental data for all the TM monoxides and properties collected in table 4.

Inspecting figure 6 in some detail, one can see that in general LSIC provides much better agreement with experiment than does LSDA, although, in more cases than not, the LSIC values are larger than the experimental data. This is definitely the case for the equilibrium lattice constants, which are also larger than the values obtained from the FSIC approach as seen in table 4 for NiO [21]. In fact, for NiO both FSIC and LSDA+U give very comparable lattice constants (respectively 4.18/4.19 Å cf [21]). The lattice constants calculated in the LSD approximation are considerably smaller than those from experiments, and therefore also from LSIC. This can be easily explained due to the fact that LSDA treats all the Ni d electrons as delocalized and responding to the same effective potential, leading to the overestimate of the bonding in NiO.

Concerning the magnetic moments calculated in LSIC, they are just spin moments, and thus do not always compare well with experiment which measure total magnetic moments,

namely, the sum of spin and orbital moments. In the earlier FSIC (LMTO–ASA) calculations, Svane and Gunnarsson evaluated not only the spin moments, but also the orbital magnetic moments for the whole TMO series [6] and they are substantial in particular for FeO and CoO. Although the orbital moments of TM ions in solids are usually quenched, in the case of TMOs, it is expected that correlation effects will preserve the orbital moments up to a certain value due to a reduction of ligand crystal field effects at the TM ion sites. For example, in CoO, the experimentally observed total magnetic moment of 3.4 μ_B [60], is quite well reproduced by FSIC with the calculated orbital moment, μ_L, of 1.19 μ_B and spin moment of 2.53 μ_B [6]. LSIC–KKR gives a slightly higher spin magnetic moment for CoO (see table 4) than obtained from FSIC (LMTO) calculations, but by comparison with experiment would still imply a substantial orbital contribution of about 0.7 μ_B for CoO. Magnetic x-ray scattering experiments of Fernandez *et al* [61] indicate that also the orbital moment in NiO is not quenched. They observe a spin moment of 1.90 μ_B and an orbital moment of 0.32 μ_B, which compares quite well with the FSIC value of 0.27 μ_B [6]. Looking across
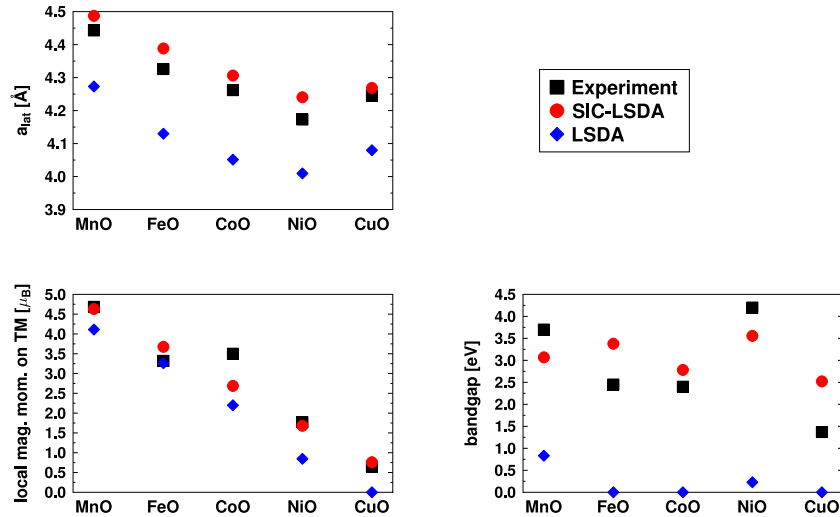
Figure 6. The calculated equilibrium lattice constants, band gaps and local magnetic moments on TM sites for the TMO series (AFII structure). The band gaps and local magnetic moments shown are those corresponding to the equilibrium lattice constant. In contrast to the experimental magnetic moments the theoretical magnetic moments are spin moments only.

the series, the spin magnetic moments obtained with LSIC–KKR are slightly higher than the moments from the full SIC calculations, which may not necessarily be due to the local SIC implementation but due to the different band structure methods used in both implementations.

The small size or lack of the band gap is what best characterizes the breakdown of the LSDA description of the physics of TMOs. Only for MnO and NiO small gaps are obtained in LSDA calculations. The LSIC approach improves the agreement with experiment dramatically and the trends across the series are predicted correctly, in line with the FSIC approaches although the LSIC values are in general larger than those from FSIC.

To summarize this section, we have to say that LSIC often overestimates the physical properties calculated here as compared to the respective experimental data. One possible reason for this may be the use of the atomic sphere approximation in KKR. While in the LMTO method ASA works quite well, due to some error cancellations, in KKR this is most likely not the case. The KKR method is based on the multiple scattering theory and invokes the so-called 'on energy-shell' formulation implying that a scattering process is finished before another one will start. With the ASA in use, this condition would have most likely not been fulfilled. Of course, more developments are needed, e.g., full potential implementation or at least the so-called ASA-muffin-tin (MT) correction [62] to check this possibility further. In this paper, however, our aim has been to demonstrate that LSIC works for correlated 3d electron systems, with more than one atom per unit cell.

6. Vacancy-induced half-metallicity in NiO

In this section we discuss an application of LSIC to study doping of NiO with cation vacancies. This has been motivated by a recent study of Ködderitzsch *et al* [10] who, using FSIC implemented in the LMTO–ASA method, showed that for

3.125% of cation vacancies in one of the Ni-sublattices of the AFII NiO realized in a supercell geometry, NiO switches from an insulator to a half-metal.

As mentioned earlier, being a Green's function method, KKR lends itself naturally to such extensions as CPA and DLM. Thus, with the present application, we aim not only to compare the LSIC–KKR and FSIC–LMTO approaches, but also explore how well CPA can reproduce the supercell results. Using CPA instead of the supercell geometry would not only reduce the computing effort but also allow access to a whole range of concentrations that would be difficult to realize in the supercell approach due to huge sizes required.

Like Ködderitzsch *et al* [10], we have used a ($2 \times 2 \times 2$) AFII supercell, comprising 32 formula units [10]. Also, the ASA radii of 2.70 au for Ni atoms and 2.16 au for oxygen atoms are the same as in the other study [10]. The concentration of 3.125% of cation vacancies has been realized by replacing a single Ni cation by an empty sphere in one of the Ni-sublattices of the supercell. To reduce computational costs, the calculations have been performed without space filling empty spheres, with the effect of decreasing the size of the band gap by about 0.3 eV as compared to the case where empty spheres were included in the basic AFII unit cell. The CPA calculations have been performed for the latter cell, but also without space filling empty spheres and the same ASA radii as for the supercell approach. To improve on the ASA in the KKR implementation, we have included the so-called ASA-MT correction [62] while in LMTO–ASA, the combined correction term has been used for this purpose [41, 42].

In figure 7, the resulting DOS for $Ni_{0.97}O$, calculated both for the supercell [LSIC (KKR)] and with CPA [LSIC (KKR–CPA)], are compared to the FSIC–LMTO–ASA calculation. In all the cases we observe a fairly convincing half-metallic state. The smearing of the CPA curve reflects both the nature of the effective medium and a small imaginary part of the energy. In addition to a qualitatively similar DOS, the total magnetic moments calculated with LSIC (KKR) method
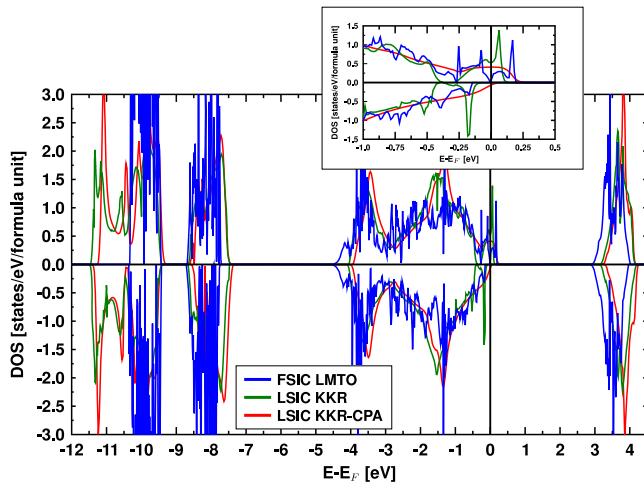
Figure 7. The spin-decomposed total density of states for NiO, calculated with LSIC–KKR–CPA for 3.125% of cation vacancies in one of the Ni-sublattices of the AFII NiO. Presented are DOS curves calculated in the supercell geometry using respectively, LSIC implemented in the KKR–ASA and FSIC implemented in LMTO–ASA. Also shown is the DOS obtained from the KKR–CPA (ASA) for the same vacancy concentration. The majority spin DOS is printed on the positive side, while the minority one on the negative side of the DOS-axis.

in both supercell and CPA approaches are exactly zero, in agreement with the FSIC (LMTO) calculations. The way the zero magnetic moment comes about is that by removing a TM cation one create moment of $-2\mu_B$, which compensates the Ni spin moment of $2\,\mu_B$.

In summary, we have demonstrated that LSIC (KKR) method provides an adequate description of the vacancy-induced half-metallicity in NiO, both with the supercell and CPA approaches. This gives us confidence that one will be able to explore the whole range of vacancy concentrations not only on one but both Ni-sublattices, concentrating on energetics and the existence and origin of half-metallicity. However, such a study lies outside the scope of the present paper and will be published elsewhere.

7. Summary and conclusions

We have presented and discussed in some detail a local implementation of the SIC–LSDA formalism in the multiple scattering theory. By applying it to 3d transition metal oxides we have demonstrated that this approach can describe trends for many physical properties of these compounds and compares well with earlier implementations of SIC–LSDA in LMTO–ASA, exploiting repeated transformations between Bloch and Wannier representations to solve the eigenvalue problem and reproduce the localized nature of TM d electrons in these compounds. With the present study we have shown that LSIC works equally well for the 3d TMOs as for the 4f systems [15]. The great potential of LSIC lies in its flexibility and ability to study various types of disorder in combination with CPA and DLM, opening up possibilities to consider thermal fluctuations and, through them, finite temperature

phase diagrams and finite temperature magnetism, including ordering temperatures [15, 16, 52]. Applying the combination of LSIC with CPA to study changes in the electronic structure of NiO induced by doping cation vacancies into Ni-sublattices, we have shown that LSIC can describe chemical disorder in addition to spin and valence disorder demonstrated in earlier applications, also at finite temperatures [15, 16, 52]. It is very encouraging that with LSIC one can study also surfaces, interfaces and even clusters on surfaces, based on the Green's functions without the need of invoking large supercell geometries. In the present paper we have explored only the ASA implementation in KKR although in the application to vacancies in NiO, the so-called ASA-MT correction has also been included [62]. However, in future, we need to perform a systematic study to compare ASA against the more appropriate MT approximation, the ASA-MT correction [62], and eventually the full potential (no shape approximation) implementation. In this paper, however, our prime goal was to explain the LSIC method and demonstrate that it works for correlated 3d electron compounds as well as for the 4f electron systems.

Acknowledgments

References

[1] Kohn W and Sham L J 1965 Self-consistent equations including exchange and correlation effects *Phys. Rev.* **140** A1133
[2] Terakura K, Oguchi T, Williams A R and Kübler J 1984 Band theory of insulating transition-metal monoxides: band-structure calculations *Phys. Rev.* B **30** 4734
[3] Terakura K, Williams A R, Oguchi T and Kübler J 1984 Transition-metal monoxides: band or Mott insulators *Phys. Rev. Lett.* **52** 1830
[4] Yamashita J and Asano S 1983 Cohesive properties of 3d transition-metal monoxides *J. Phys. Soc. Japan* **52** 3514–9
[5] Perdew J P and Zunger A 1981 Self-interaction correction to density-functional approximations for many-electron systems *Phys. Rev.* B **23** 5048
[6] Svane A and Gunnarsson O 1990 Transition-metal oxides in the self-interaction-corrected density-functional formalism *Phys. Rev. Lett.* **65** 1148
[7] Szotek Z, Temmerman W M and Winter H 1993 Application of the self-interaction correction to transition-metal oxides *Phys. Rev.* B **47** 4029
[8] Temmerman W M, Winter H, Szotek Z and Svane A 2001 Cu valency change induced by O doping in YBCO *Phys. Rev. Lett.* **86** 2435
[9] Ködderitzsch D, Hergert W, Temmerman W M, Szotek Z, Ernst A and Winter H 2002 Exchange interactions in NiO and at the NiO(100) surface *Phys. Rev.* B **66** 064434

[10] Ködderitzsch D, Hergert W, Szotek Z and
     Temmerman W M 2003 Vacancy-induced half-metallicity in
     MnO and NiO *Phys. Rev.* B **68** 125114
[11] Szotek Z, Temmerman W M and Winter H 1994
     Self-interaction corrected local spin density description of
     the $\gamma - \alpha$ transition in Ce *Phys. Rev. Lett.* **72** 1244
[12] Beiden S V, Temmerman W M, Szotek Z and
     Gehring G A 1997 Self-interaction free relativistic local spin
     density approximation: equivalent of Hund's rules in γ-Ce
     Phys. Rev. Lett. **79** 3970
[13] Strange P, Svane A, Temmerman W M, Szotek Z and
     Winter H 1999 Understanding the valency of rare earths
     from first-principles theory *Nature* **399** 756–8
[14] Petit L, Svane A, Szotek Z and Temmerman W M 2003
     First-principles calculations of $PuO_{2\pm x}$ *Science*
     301 498–501
[15] Lüders M, Ernst A, Dane M, Szotek Z, Svane A,
     Ködderitzsch D, Hergert W, Gyorffy B L and
     Temmerman W M 2005 Self-interaction correction in
     multiple scattering theory *Phys. Rev.* B **71** 205109
[16] Hughes I D, Däne M, Ernst A, Hergert W, Lüders M, Poulter J,
     Staunton J B, Svane A, Szotek Z and
     Temmerman W M 2007 Lanthanide contraction and
     magnetism in the heavy rare earth elements *Nature*
     446 650–3
[17] Szotek Z, Temmerman W M and Winter H 1991
     Self-interaction correction of localized bands within the
     LMTO–ASA band structure method *Physica* B **172** 19
[18] Temmerman W M, Svane A, Szotek Z, Winter H and
     Beiden S V 2000 On the implementation of the
     self-interaction corrected local spin density approximation
     for d- and f-electron systems *Electronic Structure and
     Physical Properties of Solids—The use of the LMTO Method*
     (*Springer Lecture notes in Physics*) (Berlin: Springer)
[19] Gyorffy B L, Pindor A J, Staunton J, Stocks G M and
     Winter H 1985 A first-principles theory of ferromagnetic
     phase transitions in metals *J. Phys. F: Met. Phys.*
     15 1337–86
[20] Anisimov V I, Solovyev I V, Korotin M A, Czyyk M T and
     Sawatzky G A 1993 Density-functional theory and NiO
     photoemission spectra *Phys. Rev.* B **48** 16929
[21] Dudarev S L, Botton G A, Savrasov S Y, Szotek Z,
     Temmerman W M and Sutton A P 1998 Electronic structure
     and elastic properties of strongly correlated metal oxides
     from first principles: LSDA $+U$, SIC–LSDA and EELS
     study of UO_2 and NiO *Phys. Status Solidi* a **166** 429–43
[22] Xiaobing F 2004 Electronic structure of MnO and CoO from
     the B3LYP hybrid density functional method *Phys. Rev.* B
     69 155107
[23] Franchini C, Bayer V, Podloucky R, Paier J and Kresse G 2005
     Density functional theory study of MnO by a hybrid
     functional approach *Phys. Rev.* B **72** 045132
[24] Tran F, Blaha P, Schwarz K and Novak P 2006 Hybrid
     exchange–correlation energy functionals for strongly
     correlated electrons: applications to transition-metal
     monoxides *Phys. Rev.* B **74** 155108
[25] Franchini C, Podloucky R, Paier J, Marsman M and
     Kresse G 2007 Ground-state properties of multivalent
     manganese oxides: density functional and hybrid density
     functional calculations *Phys. Rev.* B **75** 195128–11
[26] Anisimov V I, Zaanen J and Andersen O K 1991 Band theory
     and Mott insulators: Hubbard U instead of Stoner I *Phys.
     Rev.* B **44** 943
[27] Liechtenstein A I, Anisimov V I and Zaanen J 1995
     Density-functional theory and strong interactions: orbital
     ordering in Mott–Hubbard insulators *Phys. Rev.* B **52** R5467
[28] Anisimov V I, Aryasetiawan F and Lichtenstein A I 1997
     First-principles calculations of the electronic structure and
     spectra of strongly correlated systems: the LDA $+U$ method
     J. Phys.: Condens. Matter **9** 767

[29] Dudarev S L, Liechtenstein A I, Castell M R, Briggs G A D and
     Sutton A P 1997 Surface states on NiO(100) and the origin
     of the contrast reversal in atomically resolved scanning
     tunneling microscope images *Phys. Rev.* B **56** 4900
[30] Castell M R, Wincott P L, Condon N G, Muggelberg C,
     Thornton G, Dudarev S L, Sutton A P and
     Briggs G A D 1997 Atomic-resolution STM of a system
     with strongly correlated electrons: NiO(001) surface
     structure and defect sites *Phys. Rev.* B **55** 7859
[31] Bayer V, Franchini C and Podloucky R 2007 *Ab initio* study of
     the structural, electronic, and magnetic properties of MnO
     (100) and MnO(110) *Phys. Rev.* B **75** 035404
[32] Zhang W-B, Hu Y-L, Han K-L and Tang B-Y 2006 Pressure
     dependence of exchange interactions in NiO *Phys. Rev.* B
     74 054421
[33] Becke A D 1993 Density-functional thermochemistry. III. The
     role of exact exchange *J. Chem. Phys.* **98** 5648–52
[34] Georges A, Kotliar G, Krauth W and Rozenberg M 1996
     Dynamical mean-field theory of strongly correlated fermion
     systems and the limit of infinite dimensions *Rev. Mod. Phys.*
     68 13–125
[35] Held K 2007 Electronic structure calculations using dynamical
     mean field theory *Adv. Phys.* **56** 829–926
[36] Kunes J, Anisimov V I, Skornyakov S L, Lukoyanov A V and
     Vollhardt D 2007 NiO: correlated band structure of a
     charge-transfer insulator *Phys. Rev. Lett.* **99** 156404
[37] Aryasetiawan F and Gunnarsson O 1995 Electronic structure of
     NiO in the GW approximation *Phys. Rev. Lett.* **74** 3221
[38] Aryasetiawan F and Gunnarsson O 1998 The GW method *Rep.
     Prog. Phys.* **61** 237–312
[39] Massidda S, Continenza A, Posternak M and
     Baldereschi A 1997 Quasiparticle energy bands of
     transition-metal oxides within a model GW scheme *Phys.
     Rev.* B **55** 13494
[40] Li J-L, Rignanese G M and Louie S G 2005 Quasiparticle
     energy bands of NiO in the GW approximation *Phys. Rev.* B
     71 193102
[41] Andersen O K and Jepsen O 1984 Explicit, first-principles
     tight-binding theory *Phys. Rev. Lett.* **53** 2571
[42] Andersen O K, Pawlowska Z and Jepsen O 1986 Illustration of
     the linear-muffin-tin-orbital tight-binding representation:
     compact orbitals and charge density in Si *Phys. Rev.* B
     34 5253
[43] Soven P 1967 Coherent-potential model of substitutional
     disordered alloys *Phys. Rev.* **156** 809
[44] Stocks G M, Temmerman W M and Gyorffy B L 1978
     Complete solution of the Korringa–Kohn–Rostoker
     coherent-potential-approximation equations: Cu–Ni alloys
     Phys. Rev. Lett. **41** 339
[45] Pindor A J, Temmerman W M and Gyorffy B L 1983 KKR
     CPA for two atoms per unit cell: application to Pd and PdAg
     hydrides *J. Phys. F: Met. Phys.* **8** 1627
[46] Temmerman W M and Pindor A J 1983 The electronic structure
     of non-stoichiometric Pd-rich Pd–Ag hydrides *J. Phys. F:
     Met. Phys.* **9** 1869
[47] Fang Z, Solovyev I V, Sawada H and Terakura K 1999
     First-principles study on electronic structures and phase
     stability of MnO and FeO under high pressure *Phys. Rev.* B
     59 762
[48] Silinsky P S and Seehra M S 1981 Principal magnetic
     susceptibilities and uniaxial stress experiments in CoO *Phys.
     Rev.* B **24** 419
[49] Shull C G, Strauser W A and Wollan E O 1951 Neutron
     diffraction by paramagnetic and antiferromagnetic
     substances *Phys. Rev.* **83** 333
[50] Lloyd P and Smith P V 1972 Multiple scattering theory in
     condensed materials *Adv. Phys.* **21** 69–142

[51] Däne M 2008 Beschreibung der elektronischen struktur korrelierter systeme mittels lokaler selbstwechselwirkungskorrekturen im rahmen der vielfachstreutheorie *PhD Thesis* Martin-Luther-Universität Halle-Wittenberg, Germany

[52] Hughes I D, Däne M, Ernst A, Hergert W, Lüders M, Staunton J B, Szotek Z and Temmerman W M 2008 Onset of magnetic order in strongly-correlated systems from *ab initio* electronic structure calculations: application to transition metal oxides *New J. Phys.* **10** 063010

[53] Sawatzky G A and Allen J W 1984 Magnitude and origine of the band gap in NiO *Phys. Rev. Lett.* **53** 2339

[54] Zaanen J, Sawatzky G A and Allen J W 1985 Band gaps and electronic structure of transition-metal compounds *Phys. Rev. Lett.* **55** 418–21

[55] Temmerman W M, Svane A, Szotek Z and Winter H 1998 Applications of self-interaction corrections to localized states in solids *Electronic Density Functional Theory: Recent Progress and New Directions* ed J F Dobson, G Vignale and M P Das (New York: Plenum) p 327

[56] Schulthess T C, Temmerman W M, Szotek Z, Svane A and Petit L 2007 First-principles electronic structure of Mn-doped GaAs, GaP, and GaN semiconductors *J. Phys.: Condens. Matter* **19** 165207

[57] Freeman A J, Min B I and Norman M R 1987 *Handbook on the Physics and Chemistry of Rare Earths* vol 10, ed K A Gschneider Jr, L Eyring and S Hüfner (Amsterdam: Elsevier) pp 165–229

[58] Slater J C 1951 A simplification of the Hartree–Fock method *Phys. Rev.* **81** 385

[59] Filippetti A and Spaldin N A 2003 Self-interaction-corrected pseudopotential scheme for magnetic and strongly correlated systems *Phys. Rev.* B **67** 125109

[60] Khan D C and Erickson R A 1970 Magnetic form factor of Co^{++} ion in cobaltous oxide *Phys. Rev.* B **1** 2243

[61] Fernandez V, Vettier C, de Bergevin F, Giles C and Neubeck W 1998 Observation of orbital moment in NiO *Phys. Rev.* B **57** 7870

[62] Zhang X G and Nicholson D M C 1999 Generalized local-density approximation for spherical potentials *Phys. Rev.* B **60** 4551

[63] Sasaki S, Fujino K, Takéguchi Y and Sadanaga R 1980 *Acta Crystallogr.* A **36** 904–15

[64] Various other oxides *Numerical Data and Functional Relations in Science and Technology* 1992 (*Landoldt-Börnstein, New Series* Group III vol 27g) (Berlin: Springer)

[65] Fjellvåg H, Grønvold F, Stølen S and Hauback B 1996 *J. Solid State Chem.* **124** 52–7

[66] Schmahl N G and Eikerling G F 1968 *Z. Phys. Chem.* **62** 268

[67] Schmahl N G, Barthel J and Eikerling G F 1964 *Z. Anorg. Allg. Chem.* **332** 230–7

[68] Bowen H K, Adler D and Auker B H 1975 *J. Solid State Chem.* **12** 355–9

[69] Kim B-s, Hong S and Lynch D W 1990 *Phys. Rev.* B **41** 12227

[70] Fender B E F, Jacobson A J and Wegwood F A 1968 *J. Chem. Phys.* **48** 990

[71] Cheetham A K and Hope D A O 1983 *Phys. Rev.* B **27** 6964

[72] Roth W L 1958 *Phys. Rev.* **110** 1333

[73] Forsyth J B, Brown P J and Wanklyn B M 1988 *J. Phys. C: Solid State Phys.* **21** 2917

[74] Iskenderov R N, Drabkin I A, Emel'yanova L T and Ksendzov Ya M 1968 *Fiz. Tverd. Tela* **10** 2573

[75] van Elp J, Wieland J L, Eskes H, Kuiper P, Sawatzky G A, Groot F M F and Turner T S 1991 *Phys. Rev.* B **44** 6090

[76] Fujimori A, Minami F and Sugano S 1984 *Phys. Rev.* B **29** 5225

[77] Hüfner S, Osterwalder J, Riesterer T and Hulliger F 1984 *Solid State Commun.* **52** 793

[78] Koffyberg F P and Benko F A 1982 *J. Appl. Phys.* **53** 1173